Fluorescent Emission Enhancement by Aluminium Nanoantenna Arrays in the Near UV

N. Dorh[1], A. Sarua[2], J. Stokes[3], N. A. Hueting[1], and M. J. Cryan[1]
[1]Department of Electrical and Electronic Engineering, University of Bristol, UK
[2]H. H. Wills Physics Laboratory, School of Physics, University of Bristol, UK
[3]Department of Chemistry, University of Hull, UK

Abstract: In this paper, we demonstrate fluorescence enhancement of a laser dye, using aluminium nanoantenna arrays designed for the near UV range. A series of nanorod arrays were fabricated by focused ion beam milling then spin-coated with a dye with an intrinsic quantum yield in the range 0.5-0.6. Scanning confocal photoluminescence measurements of the arrays show up to 1.9x enhancement of the fluorescence signal compared to the reference on glass. The observed near UV fluorescence enhancement is affected by the relatively high intrinsic quantum yield of the dye and coupling to an array mode. FDTD modelling predicts strong dependence of the emission on angle, with maximum emission at high angles with respect to normal. The model predicts that using a lens with a numerical aperture of 0.9 would lead to an enhancement of up to ~6x enhancement.

I. Introduction

Aluminium plasmonics in the ultraviolet (UV) spectral region is the subject of much recent research activity[1-10]. Aluminium has a relatively high density of free electrons which results in a very short plasma wavelength ($\lambda_p = 84.2\ nm$) [1] and by extension, the ability to support surface plasmons in the UV. Interband transitions of aluminium, unlike that of many other metals, are spectrally localised[11] and therefore permit surface plasmons over a much broader wavelength range. Similarly, other members of group III, such as indium (In)[10], and semi-metals[12] in general, could also support plasmonic activity in the UV. However, the low cost of aluminium, its natural abundance and widespread use in commercially-established fabrication processes makes it highly attractive for new applications. Fluorescence enhancement in the visible and near infrared [13-15] has been a major focus of nanoantenna research, however, the UV region is of special interest, particularly for medical and biotechnology applications. This is because many important bio-molecules fluoresce under UV excitation [8, 16], albeit with low efficiency. Aluminium based plasmonics has extended existing research interests, to include resonant enhancement of UV fluorescence[4, 8, 17], enhanced photoluminescence from AlGaN quantum well UV LEDs[18], and structural colour [19]. In [5], we studied a 2 x 2 aluminium dipole nanoantenna array, demonstrating that unique radiation patterns and enhancement can be produced for varying combinations of emitter polarisations, which could be useful for sub-diffraction limit imaging and quantum optics. As in our earlier work, here, we use a higher order resonant mode of the antenna in order to achieve resonance in the UV spectral region, which is of a particular relevance for resonant enhancement of fluorescence.

Gérard and Gray[1] suggest that emission of a fluorophore can be enhanced via three interconnected mechanisms: local enhancement of the excitation field by the nanoantenna, Purcell enhancement[20, 21] of the fluorophore and improved coupling to the detector due to the increase in directivity[14] provided by the nanoantennas. In this work, we explore metal enhanced fluorescence using the latter two effects; an array of aluminium nanoantennas is designed such that the array resonance overlaps dye emission. There have been a number of experimental studies which demonstrate extremely narrow Surface Lattice Resonances [22-26] which arise when regular arrays of nanoparticles support diffractive coupling of individual plasmon resonances. However, work by Shi *et al*[27], shows that while these surface lattice resonances are spectrally narrow, they exhibit angular dispersion. In a practical terms, this can have a significant impact on the measured enhancement. In this paper, we quantify the enhancement using scanning confocal photoluminescence (PL) measurements, comparing the emission over the nanoantennas to that over the glass substrate. A similar approach was recently used by Jha *et*

al[4], demonstrating 80x enhancement of intrinsic, low quantum yield (QY), adenine UV fluorescence (QY~10^{-4}). In [17], Jaio *et al* demonstrate a 3.5x lifetime reduction for high efficiency UV laser dye (QY=0.88) using aluminium nano-apertures whilst in [7], Mupparapu *et al* do not explicitly state the intrinsic quantum yield of the dye used but noted UV fluorescence enhancement in the region of ~1.2x.

The first section of this paper introduces the design and fabrication of aluminium nanoantenna arrays. The second and third sections address the experimental methods and results, respectively. In the final section, we present the FDTD model of the photoluminescence measurements and discussion.

IIa. Design and Fabrication

FDTD modelling was used to design the nanorod geometry with a resonance near 400 nm. The structure is shown in Fig 1a and consists of a single aluminium block of length, l = 220 nm, width, w = 50 nm, height, d = 50 nm, set on a glass substrate of thickness, s and refractive index, n = 1.5. The length of the nanoantenna determines the resonant wavelength, which is known to scale linearly [15, 28]. In this model, we simulate the interaction of dye molecules with the nanoantennas and represent a single dye molecule by a simple dipole source. In reality, the fluorescent dye molecules will have a random orientation with respect to the antennas, however, in order to simplify the analysis we focus on two scenarios: the antennas can either be centre- or end-fed as shown in Fig 1a. For optimum coupling the electric dipole is $\boldsymbol{E_x}$ polarised in the end-fed configuration and $\boldsymbol{E_y}$ polarised in the centre fed configuration. In Fig 1b, we plot the power enhancement for both configurations with the electric dipole 15 nm away from the single aluminium nanorod antenna. Here, enhancement is the net power through a plane 50 nm above the nanoantenna-substrate system normalised to the power that would have been emitted through the plane by the source in free space. Fig 1b also includes the enhancement for infinite centre- and end-fed nanorod nanoantenna arrays; calculated by using periodic boundary conditions in the lateral directions. The array was defined by a horizontal pitch, $l_x = 400\ nm$ and vertical pitch, $l_y = 300\ nm$; this allows electromagnetic coupling to occur between elements, such that array effects could be investigated. In the end-fed configuration, a single nanoantenna generates a peak enhancement of 1.4x at 451 nm, but the centre-fed configuration generates peak enhancement of 1.6x at 428 nm. In the case of the array, as the localised plasmon modes of the elements couple to the surface lattice mode, we observe a narrow Fano type resonance[23] for both excitation configurations, blue-shifted (~395 nm) with respect to the individual resonances (Fig 1b). The main difference between the array resonances is the centre-fed array produces a peak enhancement of 3.3x while the end-fed configuration produces 2x peak enhancement. As noted above the individual element resonances correspond to higher order modes of the nanoantenna geometry, which give rise to off-normal far-field radiation patterns[29]. Fig 1c shows the transverse cross-section through the far field radiation patterns in the x-z plane for the single antenna and array case for each configuration. In the PL measurements presented in latter sections, a 2 µm laser spot illuminates the array; based on the array pitch, this covers a roughly 6 x 4 portion array. The array projections in Fig 1c are therefore based on a 6 x 4 array illuminated by a Gaussian spot. In physical terms, this translates to a 6 x 4 array excited within a much larger array[30], as is the case with the results presented in subsequent sections. The centre-fed mode ($\lambda = 428\ nm$) has a symmetric pattern in x-z plane with emission maxima at ± 25° and a minimum at normal. The end fed, ($\lambda = 451\ nm$) exhibits a similar pattern but is asymmetric about the normal due to the asymmetry introduced by the position of excitation. The maximum peak emission is at -35° and a smaller peak at +28° for single antenna. Strong coupling and focusing effects in the array result in a change in direction of emission and significantly narrower emission peaks. The centre-fed array has main emission peaks at ±64°and a weaker side lobe at normal. The end-fed array also has its main emission peak at -64° and two lobes at 4° and 67°. The appearance of a side lobe near normal for both configurations is likely as a result of the combination of the far field of the single nanoantenna and the surface mode to which it couples in the array.

(a)

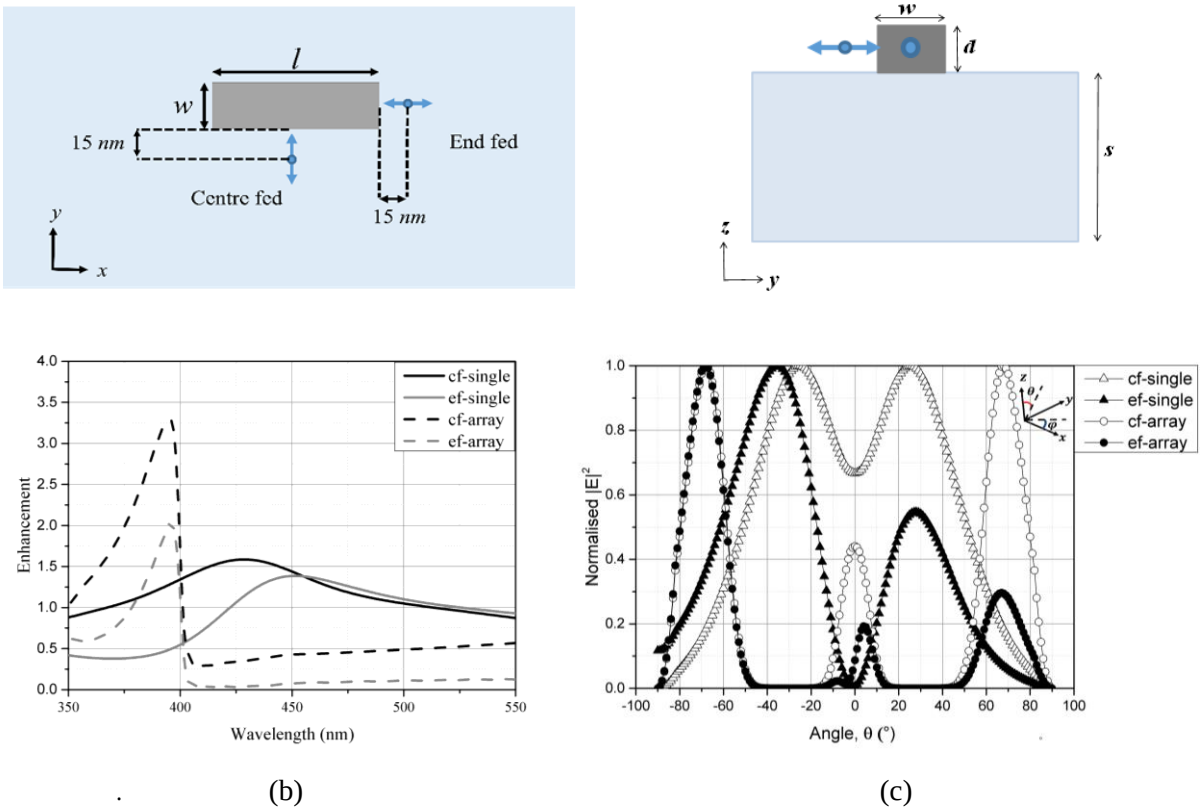

. (b) (c)

Figure 1: (a) Nanorod antenna element design length, *l*=220 nm, width, *w*=50 nm, height, *d*= 50 nm and glass thickness, *s* and refractive index, *n* = 1.5; For optimum coupling the 350-550 nm dipole is E_x polarised in the end fed configuration and E_y polarised in the centre fed configuration. (b) Enhancement for single and infinite array of aluminium nanorod nanoantennas in the end-fed (ef) and centre-fed (cf) configurations. (c) Transverse section through far field radiation pattern (total E field) of a single and 6 x 4 subset of infinite arrays of aluminium nanorod nanoantennas at resonance in the end (ef) and centre fed (cf) configurations for azimuthal angle $\varphi = 0$. Each radiation pattern has been normalised to its respective maximum.

IIb Fabrication

Fabrication technology has been one of the major challenges in nanoantenna research, since desired dimensions are in the order of tens of nanometres. Recent advances in fabrication methods have introduced several new techniques, such as nano-imprint lithography[31], two photon lithography[32], and laser interference lithography[33] and improvements have been made in established methods, like focused ion beam milling and electron beam lithography [34, 35]. Focused ion beam (FIB) milling is particularly useful as it lends itself to rapid prototyping and with relatively well defined geometries.

A series of 4 different nanoantenna arrays (A1-4) as described in Table 1 were fabricated by FIB milling on commercially acquired (EMF Corp) 50 nm aluminium on glass substrates. A patterned region, A5, consisting of rough aluminium horizontal strips, similar to a grating, was also included as an additional reference. Fig 2 shows SEM images of arrays A1-4, the arrays were designed to have nominally identical nanorod elements. It can be seen that the processing was less precise with A4 which has a central discontinuity in the array. All arrays were surrounded by an area of exposed glass with the aluminium layer removed and a 5 µm wide etched groove as a border, for increased visibility.

Arrays A1-4 were designed such that the number of columns, *n*, was kept fixed, while varying the number of rows, *m*. The pitch was kept at 400 nm horizontally and 300 nm vertically for all arrays. The entire array occupied an area of roughly 4.6 x 3.4 µm at the centre of a 10 x 10 µm region of exposed glass.

Array Label	Number of Rows, *m*	Number of Columns, *n*
A1	10	12
A2	8	12
A3	12	12
A4	11	12
A5	n/a	n/a

Table 1: Array dimensions

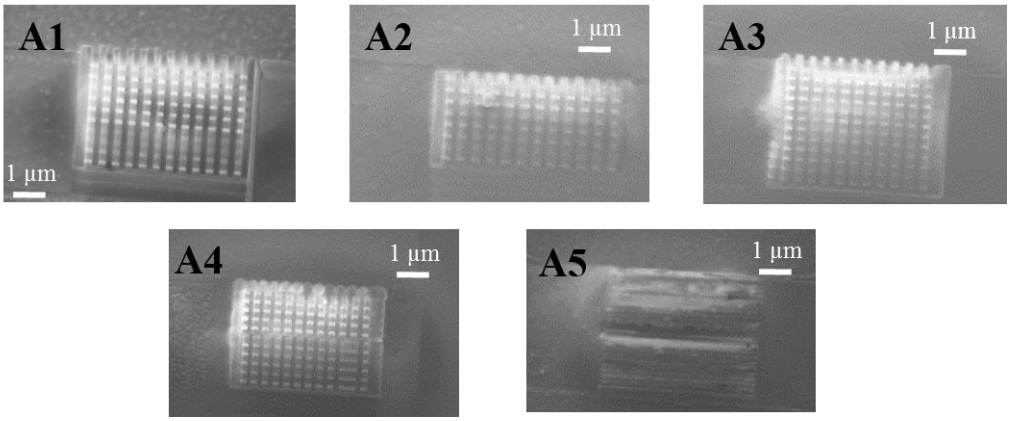

Figure 2: SEM image of aluminium nanorod arrays A1-4 and "grating" A5, with a series of horizontal rough aluminium strips. Array horizontal pitch, $l_h = 400\ nm$ and vertical pitch, $l_v = 300\ nm$ and nanontenna geometry is nominally *l*= 220nm, *w*=50nm. The array sits on a 1 mm thick glass substrate.

III.a Experimental Methods

Exalite 392E dye (Exciton Inc.) was used as a local emitting source for the nanoantenna arrays. It is highly stable, has an expected intrinsic quantum yield of ~0.5-0.6[36] and was pumped by a 325 nm He-Cd laser source. Exalite 392E has its peak emission at 392 nm, making it useful for interacting with the resonance of the nanoantenna array. The solvent for this particular dye is ethylene glycol, this is highly viscous and removes the need for mixing the dye with polymers such as poly-methyl methacrylate (PMMA).

A 1.73 mM solution of Exalite 392E in ethylene glycol was prepared by sequential dilution. The solution was then pipetted on to the nanoantenna sample and then spin coated. The dye covered sample was spun at 500 rpm for 45s, then 5000 rpm for 30s. The low rpm spin allowed the solution to spread uniformly over the entire surface and the higher rpm spin reduced the thickness of the layer. Atomic Force Microscopy (AFM) of the sample revealed the dye layer thickness to be in the region of 50 nm.

III.b Fluorescence Measurements

The function of the nanoantenna is to enhance the dye emission; thus, a photoluminescence (PL) measurement is a fairly straightforward way to investigate this process. Fig 3 depicts the UV PL line scan measurements performed. A 325 nm laser beam is focused into an approximately 2 µm diameter spot on the sample by a 0.4 NA, 40x UV microscope objective lens and emission is collected by the same lens.

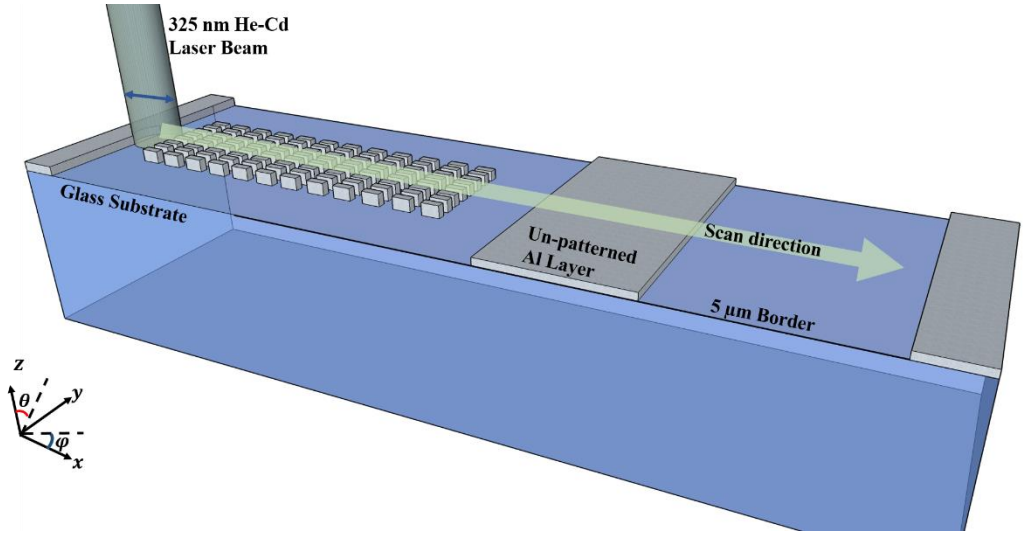

Figure 3: Line scan measurements; PL intensity measurements (between 390 nm and 410 nm) carried out while scanning across selected regions of the sample. Typically the line spanned the border, aluminium layer and array, the blue double arrow indicates the (E_x) polarisation of the laser light. (not to scale)

The resulting spatial intensity profile or line scan comprises intensity measurements over the 379-400 nm spectral window, taken in 1 µm steps, across the middle of each array, parallel to the long axis of the nanoantennas. The line scans are sufficiently long to span the array, the un-patterned aluminium and the border. It is worth noting that each measurement point along the line scan takes about 10s, and the intensity signal is collected from an illuminated spot in a solid angle defined by the NA of collection lens. These two factors need to be taken into account during modelling and will be discussed later.

IV. Results and Discussion

Fig 4 shows the typical PL spectrum of the Exalite dye on the glass substrate. The measured dye emission peak lies at 392 nm with an asymmetric line shape and has a linewidth (FWHM) of about 70 nm. Similar spectra were collected over the nanoantenna array, which is likely due to the proximity of the dye emission peak (392 nm) and the expected array resonance (395 nm).

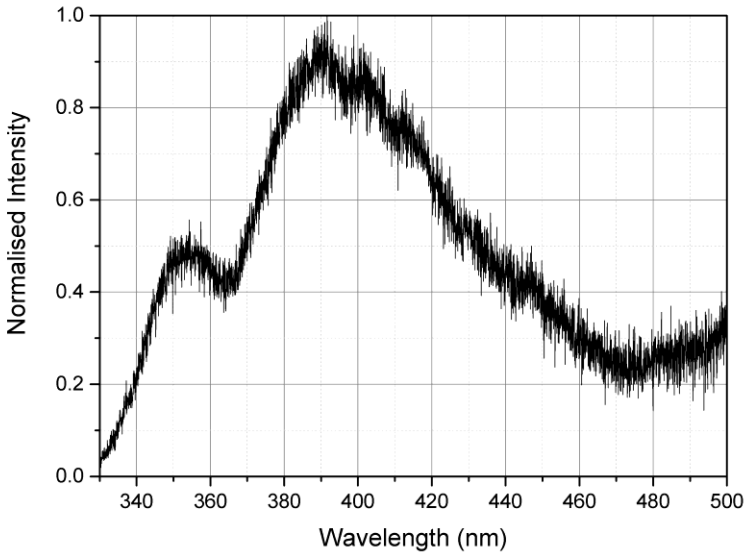

Figure 4: Normalised dye emission spectrum measured at the 5 µm border

Fig 5a shows the results of the line scans across the arrays. The line scan has been normalised to the peak emission over the glass substrate area from the border region in each scan. Two peaks emerge from the scan; the first, smaller peak appears scanning over the border/glass region and the second, higher peak appears over the nanoantenna array; relatively little emission is observed everywhere else. The emission over the unpatterned aluminium layer was likely quenched [37, 38] by the metal layer. From this data, we extract the peak enhancement defined as peak intensity over the nanoantenna array normalised to the peak emission over the border; plotted in Fig 5b. Overall, arrays A1, 2 and 3 give very similar performance, achieving 1.6 - 1.9x enhancement of fluorescence signal. Enhancement from A4 was significantly lower and more similar to the "grating" reference A5. We believe this is due to the fabrication defects in A4 reducing the effectiveness of the array. In the following sections, we develop a FDTD based model of the scanning PL measurements and discuss the overall enhancement with respect to recent literature and the narrow spread of enhancement factors.

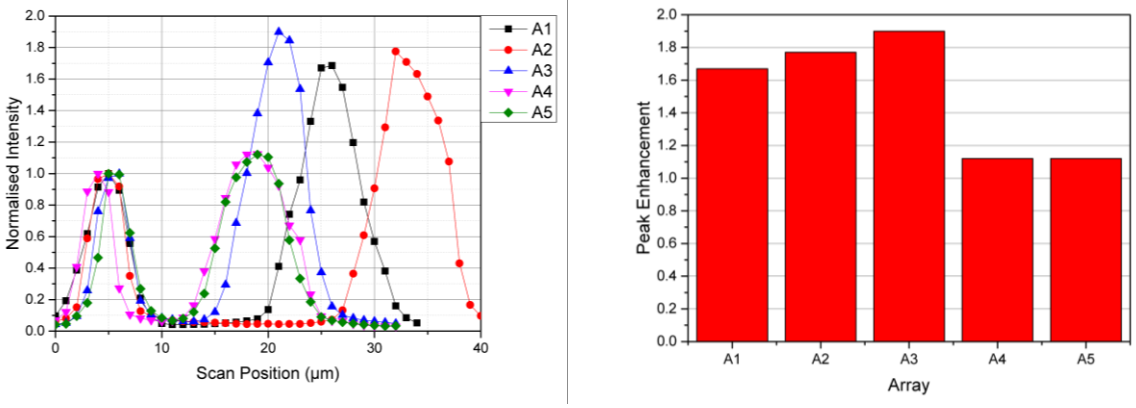

(a) (b)

Figure 5: (a) Normalised line scans for arrays A1-4 and A5; intensity normalised to the peak emission over the border region for each scan (b) Peak enhancement observed over each array; peak intensity over the array is normalised to the peak intensity over the border/glass

Figure 6 illustrates the FDTD based model [39] of the scanning measurement developed in this work. It comprises the arrays A1-4 as described in Table 1, each made of identical aluminium nanoantennas (see Fig 2) and A5, modelled as a 12 x 300 nm period aluminium grating. The nanoantenna arrays were excited by a 2D array of electric dipole sources (Fig 6 inset) with uniform pitch $l_h = 400\ nm$ and $l_v = 300\ nm$, such that the nanoantennas are centre-fed as shown in Fig 1. A uniform 1 nm mesh was selected so that a satisfactory balance of accuracy and convergence was achieved. Electric and magnetic field data is collected using a 2 μm x 2 μm planar monitor 100 nm above the array surface, scanned across the simulation region in 1 μm steps, similar to the PL measurements. At each point, a near-to-far field projection creates a half space radiation pattern, the intensity of which is integrated over a cone defined by half-angle $\theta_{NA} = sin^{-1}\left(\frac{NA}{n}\right)$; NA is the numerical aperture of the lens used (0.4) and *n* the refractive index (*n* = 1).

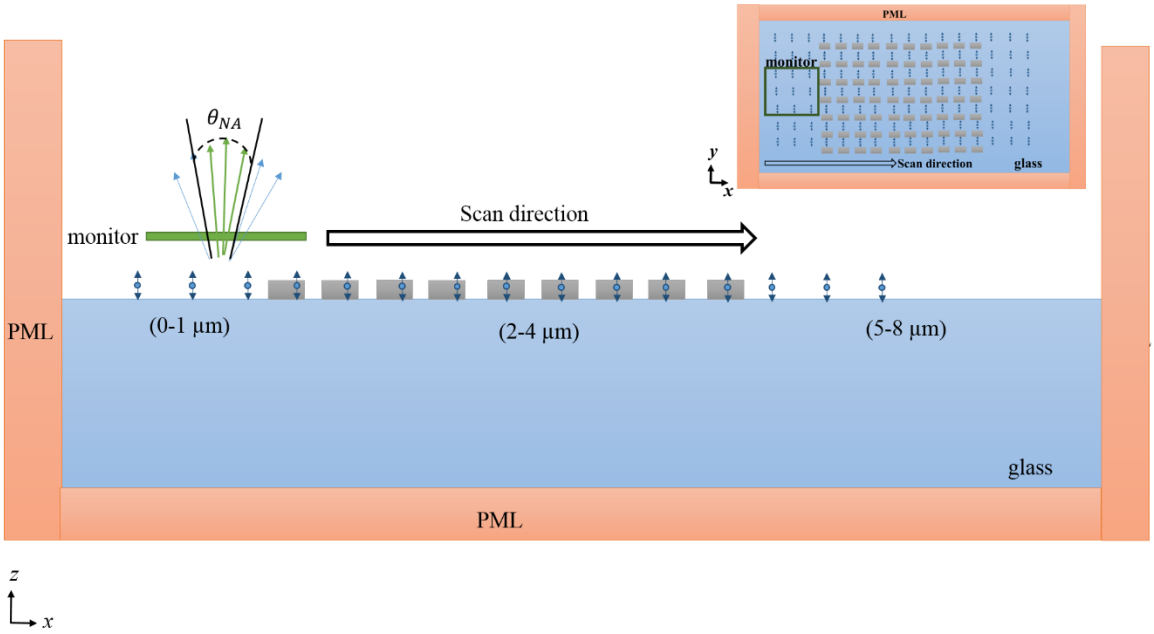

Figure 6: FDTD model of scanning PL measurement; a 2 µm x 2 µm planar monitor, 100 nm above the array collects the electric and magnetic field data in 1 µm steps. After near-to-far field conversion, the intensity in the far field is integrated over a solid angle, dictated by the NA of the measurement lens for wavelengths from 379 nm - 400 nm. The result is integrated over the wavelength range and presented as a spatial intensity profile (line scan).

The result is a series of emission spectra at each measurement location, shown in Fig 7a for the range used in PL line scans. At scan positions 0-1 µm, the planar monitor is above the glass substrate (see Fig 7); the array occupies the region between 2 and 4 µm. Beyond this region (5-8 µm), the monitor is again above the glass. Fig 7a shows that, as expected, the maximum intensity occurs over the nanoantennas and drops away when over the glass, as measured. To compare this with the line scan measurement, the intensity in the simulated emission spectrum, was integrated over the 379 -400 nm spectral region, the result for A1 is shown in Fig 7b.

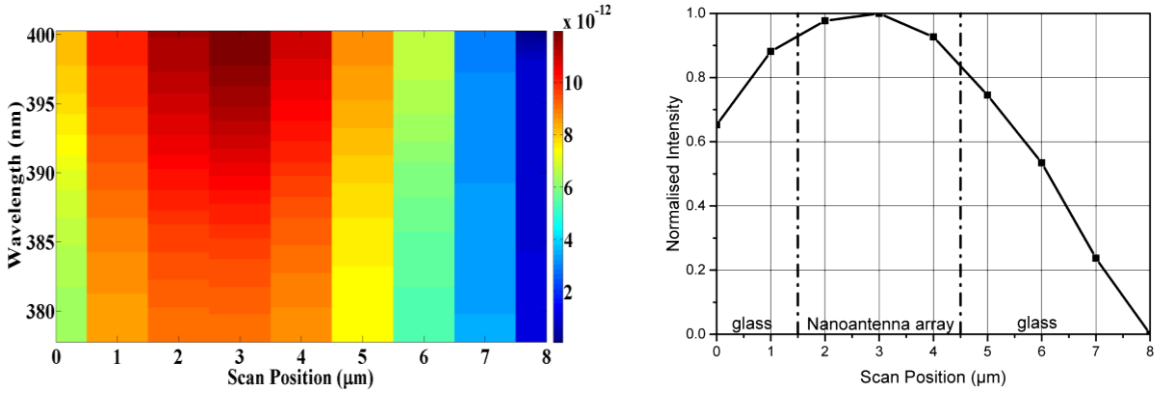

(a) (b)

Figure 7: (a) Simulated spectra for 10 x 12 array (A1); at scan points below 2 µm the planar monitor is above the glass substrate and above the array for the scan points between 2 and 4 µm. From 5 µm the monitor is above the glass substrate and moving towards the PML boundary. (b) Normalised spatial intensity profile (line scan) integrated from 379 nm -400 nm for 10 x 12 (A1).

In both the measurement (Fig 5) and FDTD model (Fig 7b), the highest intensity is recorded at the centre of the nanoantenna array. A1, A2 and A3 produce almost identical simulated line scans, this is linked to the sampling nature of the measurement and will be discussed in more detail in the next

section. It is also worth noting that, in practice, the dye molecules will be randomly oriented and distributed over the sample surface. Different emission pattern modes may appear based on the relative position and orientation of the dye molecules and antennas, which could significantly impact the observed radiation pattern and enhancement generated from the nanoantennas[5].

Fig 8 shows a comparison of the enhancement for arrays A1-A5 calculated from the model and from the measured results. Overall, the enhancement factors predicted by FDTD were almost double those calculated from measurements and they exhibit a narrower spread from one array to the next, than measurement. In the FDTD model, all the array elements are ideal, identical and the emitters are all co-polarised with the nanoantennas which led to larger enhancement factors and narrower spread than measured in the real arrays. A1-4 all produced enhancements in the range of ~3.2x; A5 produced ~2.4x. These observations suggest that low measured enhancement of A4 with respect to the other nanoantenna arrays was due to the fabrication defects and indicates the additional enhancement which can be achieved from the resonant nanoantenna arrays.

Overall both FDTD and the measurements predict that, given the experimental conditions, the resulting enhancement has relatively narrow spread across the different arrays and is relatively low. The narrow spread of enhancement factors is a direct reflection of the sampling nature of the scanning PL measurement; the emission is collected within a fixed spot size over a finite numerical aperture. Thus, in the model, identical geometries separated by an identical pitch, under the same excitation conditions should produce the same enhancement. However, the real structures would be subject to variations in geometry and native oxide layers which likely caused the differences between enhancement factors calculated from the measurements. In general, this measurement process samples a subset of the arrays. This makes direct comparison enhancement metrics across arrays with different design parameters non-trivial. Except in the cases such as presented in this work, where arrays were nominally identical, appropriate scaling between results from different works or arrays would be required for a meaningful comparison; Auguié and Barnes[23] noted a similar observation. .

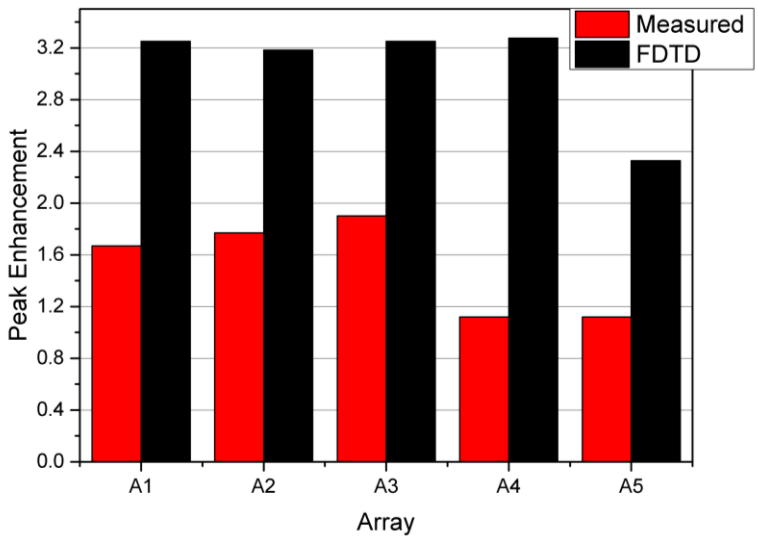

Figure 8: Enhancement ratios calculated from the measured results in Fig 6, and from the FDTD modelling for 10 x 12 array (A1), 8 x 12 array (A2), 12 x 12 array (A3) and 11 x 12 array (A4) and a 300 nm period grating (A5), shown in inset

Additionally, for emitters with high QY, opportunities for achieving a high net fluorescence enhancement is inherently limited. This is because the fluorescence enhancement is dependent on a reduction of the fluorescence lifetime, and given the emitter is already efficient, there is little room for any further reduction. The entire mechanism for achieving a net fluorescence enhancement is non-trivial and dependents on a number of interconnected processes; a more detailed discussion on the relationship

between the QY and enhancement can be found in [17, 40]. Nonetheless, we believe that there is still potential for a significant net fluorescence enhancement through the increased directivity of the array, however, the ability to experimentally observe this enhancement in the current experiment will be impacted by angular dispersion associated with the lattice mode and individual element radiation patterns.

The higher order mode for a single aluminium nanorod antenna element (shown in Fig 1b) produces emission patterns with main lobes pointing around ±25°, which shifts to even steeper angles for arrays. The PL intensity measured with the objective lens is then limited by the NA of the lens used ($\theta_{NA} = 23.6^{o}$). Hence, the PL measurements with relatively low NA are not able to capture the full emission pattern of the array. To illustrate this, Fig. 9a shows the far field radiation pattern at the array resonance wavelength 395 nm in the centre-fed configuration. The highlighted region shows the collection cone determined by the 0.4 NA lens. The weaker side lobe at normal is fully collected by the lens but the main peaks are completely out of the range.

It is therefore expected that, using higher NA lenses or performing angle resolved PL measurements, a higher enhancement figure can be obtained. To support this inference, we use the FDTD model of the PL measurement for the array A2 and reference pattern A5, and increase the collection cone, which effectively represents an increase in NA. Figure 9b shows that increasing the NA, increased the calculated enhancement for both A2 and A5, however, the difference in enhancement between the two samples increases non-linearly with NA. Further, it shows that up to ~6x enhancement can be expected for a NA of 0.9. Given the relatively high intrinsic quantum yield of Exalite dye, this predicted enhancement factor places the results on par with the findings of Jiao *et al*[17], and suggests that even higher enhancement factor is possible than presented by Jha *et al*[4], if an NA larger than 0.4 is used. These results pose significant implications for bio-imaging and bio-sensing applications in the UV.

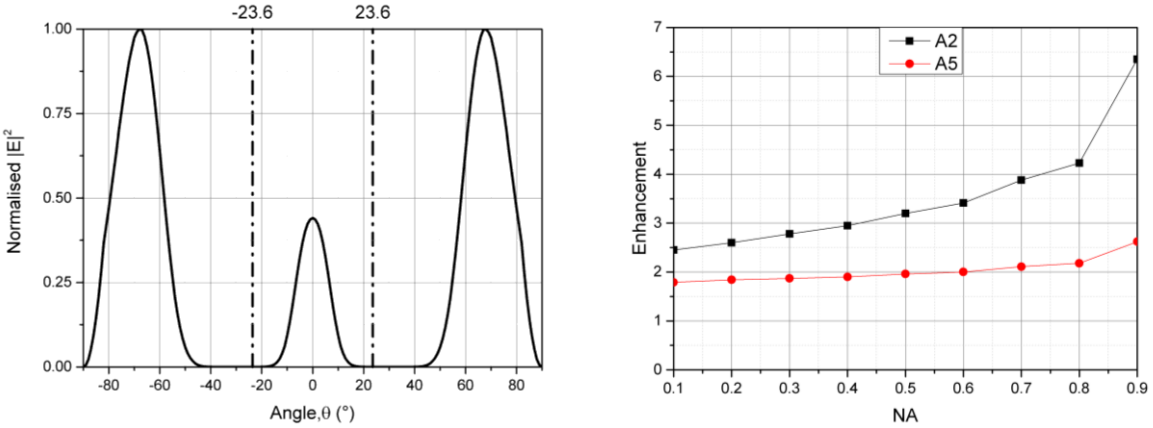

(a) (b)

Figure 9: Far Field radiation pattern for the centre fed array at 395 nm resonance, blue segment highlights the collection cone defined by the 0.4 NA lens (b) Enhancement vs numerical aperture (NA) calculated using FDTD for array A2 and region A5

Acknowledgements: The authors acknowledge funding from ABB Corporate Research.

V. Conclusions

We used FDTD modelling to design an array of aluminium nanoantenna arrays such that it produces a Fano-type lattice resonance at 395 nm. A series of arrays were fabricated by FIB milling and spin coated with laser dye Exalite 392E (emission peak 392 nm, QY~0.5-0.6). Scanning PL measurements of the array revealed enhancement factors up to 1.9x. It is believed that the relatively high QY of the dye and

dispersion associated with the lattice resonance inherently limits the observable enhancement, with a low NA lens. Using FDTD, we show that the main emission peaks of the array lie at steep angles and up to ~6x enhancement can be observed if the main lobes of radiation pattern are collected. Future work will investigate the use of the highly directional emission patterns observed here, for bio-sensing and bio-imaging applications in the UV.

References

1. D. Gérard, and S. K. Gray, "Aluminium plasmonics," Journal of Physics D: Applied Physics **48**, 184001 (2015).
2. M. W. Knight, L. Liu, Y. Wang, L. Brown, S. Mukherjee, N. S. King, H. O. Everitt, P. Nordlander, and N. J. Halas, "Aluminium Plasmonic Nanoantennas," Nano Letters **10**, 6000-6004 (2012).
3. J. Martin, M. Kociak, Z. Mahfoud, J. Proust, D. Gérard, and J. Plain, "High-Resolution Imaging and Spectroscopy of Multipolar Plasmonic Resonances in Aluminum Nanoantennas," Nano Letters **14**, 5517-5523 (2014).
4. S. K. Jha, N. Mojarad, M. Agio, J. F. Löffler, and Y. Ekinci, "Enhancement of the intrinsic fluorescence of adenine using aluminum nanoparticle arrays," Optics Express **23**, 24719-24729 (2015).
5. N. Dorh, J. Stokes, and M. J. Cryan, "Polarization and mutual coupling effects in aluminum nanoantenna arrays," J. Opt. Soc. Am. B **32**, 721-729 (2015).
6. X. Jiao, and S. Blair, "Optical antenna design for fluorescence enhancement in the ultraviolet," Optics Express **20**, 29909-29922 (2012).
7. R. Mupparapu, K. Vynck, I. Malfanti, S. Vignolini, M. Burresi, P. Scudo, R. Fusco, and D. S. Wiersma, "Enhanced downconversion of UV light by resonant scattering of aluminum nanoparticles," Opt. Lett. **37**, 368-370 (2012).
8. M. H. Chowdhury, K. Ray, S. K. Gray, J. Pond, and J. R. Lakowicz, "The use of aluminum nanostructures as platforms for metal enhanced fluorescence of the intrinsic emission of biomolecules in the ultra-violet," Proceedings - Society of Photo-Optical Instrumentation Engineers **7577**, 75770O (2010).
9. K. Ray, M. H. Chowdhury, and J. R. Lakowicz, "Aluminum Nanostructured Films as Substrates for Enhanced Fluorescence in the Ultraviolet-Blue Spectral Region," Analytical Chemistry **79**, 6480-6487 (2007).
10. M. B. Ross, and G. C. Schatz, "Aluminum and Indium Plasmonic Nanoantennas in the Ultraviolet," The Journal of Physical Chemistry C **118**, 12506-12514 (2014).
11. A. D. Rakić, "Algorithm for the determination of intrinsic optical constants of metal films: application to aluminum," Appl. Opt. **34**, 4755-4767 (1995).
12. J. M. McMahon, G. C. Schatz, and S. K. Gray, "Plasmonics in the ultraviolet with the poor metals Al, Ga, In, Sn, Tl, Pb, and Bi," Physical Chemistry Chemical Physics **15**, 5415-5423 (2013).
13. Z. Weihua, D. Fei, L. Wen-Di, W. Yuxuan, H. Jonathan, and Y. C. Stephen, "Giant and uniform fluorescence enhancement over large areas using plasmonic nanodots in 3D resonant cavity nanoantenna by nanoimprinting," Nanotechnology **23**, 225301 (2012).
14. J. L. Stokes, A. Sarua, J. R. Pugh, N. Dorh, J. W. Munns, P. G. Bassindale, N. Ahmad, A. J. Orr-Ewing, and M. J. Cryan, "Purcell enhancement and focusing effects in plasmonic nanoantenna arrays," J. Opt. Soc. Am. B **32**, 2158-2163 (2015).
15. E. Wientjes, J. Renger, A. G. Curto, R. Cogdell, and N. F. van Hulst, "Strong antenna-enhanced fluorescence of a single light-harvesting complex shows photon antibunching," Nat Commun **5** (2014).
16. I. Saadi, M. Borisover, R. Armon, and Y. Laor, "Monitoring of effluent DOM biodegradation using fluorescence, UV and DOC measurements," Chemosphere **63**, 10 (2005).
17. X. Jiao, E. M. Peterson, J. M. Harris, and S. Blair, "UV Fluorescence Lifetime Modification by Aluminum Nanoapertures," ACS Photonics **1**, 1270-1277 (2014).

18. N. Gao, K. Huang, J. Li, S. Li, X. Yang, and J. Kang, "Surface-plasmon-enhanced deep-UV light emitting diodes based on AlGaN multi-quantum wells," Scientific Reports **2**, 816 (2012).
19. S. J. Tan, L. Zhang, D. Zhu, X. M. Goh, Y. M. Wang, K. Kumar, C.-W. Qiu, and J. K. W. Yang, "Plasmonic Color Palettes for Photorealistic Printing with Aluminum Nanostructures," Nano Letters **14**, 4023-4029 (2014).
20. E. M. Purcell, "Spontaneous emission probabilities at radio frequencies," Phys. Rev. **69**, 681 (1946).
21. A. F. Koenderink, "On the use of Purcell factors for plasmon antennas," Opt. Lett. **35**, 4208-4210 (2010).
22. V. G. Kravets, F. Schedin, and A. N. Grigorenko, "Extremely Narrow Plasmon Resonances Based on Diffraction Coupling of Localized Plasmons in Arrays of Metallic Nanoparticles," Physical Review Letters **101**, 087403 (2008).
23. B. Auguié, and W. L. Barnes, "Collective Resonances in Gold Nanoparticle Arrays," Physical Review Letters **101**, 143902 (2008).
24. A. I. Väkeväinen, R. J. Moerland, H. T. Rekola, A. P. Eskelinen, J. P. Martikainen, D. H. Kim, and P. Törmä, "Plasmonic Surface Lattice Resonances at the Strong Coupling Regime," Nano Letters **14**, 1721-1727 (2013).
25. V. Giannini, G. Vecchi, and J. Gómez Rivas, "Lighting Up Multipolar Surface Plasmon Polaritons by Collective Resonances in Arrays of Nanoantennas," Physical Review Letters **105**, 266801 (2010).
26. G. Vecchi, V. Giannini, and J. Gómez Rivas, "Shaping the Fluorescent Emission by Lattice Resonances in Plasmonic Crystals of Nanoantennas," Physical Review Letters **102**, 146807 (2009).
27. L. Shi, T. K. Hakala, H. T. Rekola, J. P. Martikainen, R. J. Moerland, and P. Törmä, "Spatial Coherence Properties of Organic Molecules Coupled to Plasmonic Surface Lattice Resonances in the Weak and Strong Coupling Regimes," Physical Review Letters **112**, 153002 (2014).
28. G. W. Bryant, F. J. García de Abajo, and J. Aizpurua, "Mapping the Plasmon Resonances of Metallic Nanoantennas," Nano Letters **8**, 631-636 (2008).
29. T. H. Taminiau, F. D. Stefani, and N. F. van Hulst, "Optical Nanorod Antennas Modeled as Cavities for Dipolar Emitters: Evolution of Sub- and Super-Radiant Modes," Nano Letters **11**, 1020-1024 (2011).
30. "Far field projections - Periodic Structures," http://docs.lumerical.com/en/solvers_far_field_projections_periodic.html.
31. N. Kooy, K. Mohamed, L. T. Pin, and O. S. Guan, "A review of roll-to-roll nanoimprint lithography," Nanoscale Res Lett **9**, 1-13 (2014).
32. D. Yang, S. J. Jhaveri, and C. K. Ober, "Three-Dimensional Microfabrication by Two-Photon Lithography," MRS Bulletin **30**, 976-982 (2005).
33. J.-M. Park, K. S. Nalwa, W. Leung, K. Constant, S. Chaudhary, and K.-M. Ho, "Fabrication of metallic nanowires and nanoribbons using laser interference lithography and shadow lithography," Nanotechnology **21**, 6 (2010).
34. A. A. Tseng, "Recent Developments in Nanofabrication Using Focused Ion Beams," Small **1**, 924-939 (2005).
35. A. A. Tseng, C. Kuan, C. D. Chen, and K. J. Ma, "Electron beam lithography in nanoscale fabrication: recent development," Electronics Packaging Manufacturing, IEEE Transactions on **26**, 141-149 (2003).
36. "Private communication with Exciton Inc," (2015).
37. K. H. Drexhage, "Influence of a dielectric interface on fluorescence decay time," Journal of Luminescence **1–2**, 693-701 (1970).
38. G. W. Ford, and W. H. Weber, "Electromagnetic interactions of molecules with metal surfaces," Physics Reports **113**, 195-287 (1984).
39. "Lumerical FDTD Solutions," (Lumerical Solutions, Inc).
40. J. B. Khurgin, G. Sun, and R. A. Soref, "Electroluminescence efficiency enhancement using metal nanoparticles," Applied Physics Letters **93**, - (2008).